


## MATERIALS SCIENCE

## Rock-salt and helix structures of silver iodides under ambient conditions

Hongyang Huang<sup>1</sup>, Jinying Zhang <sup>1,\*</sup>, Yifan Zhang<sup>2</sup>, Chengcheng Fu<sup>1</sup>,  
Jialiang Huang<sup>1</sup>, Yonghong Cheng<sup>1</sup>, Chunming Niu<sup>1</sup>, Xinluo Zhao<sup>2</sup>  
and Hisanori Shinohara<sup>3</sup>

## ABSTRACT

Many different phase structures have been discovered for silver iodides. The  $\beta$  and  $\gamma$  phases were found to be the most common ones at ambient conditions, while the rock-salt phase was found to be stable under pressures between 400 MPa and 11.3 GPa. Recently, the  $\alpha$  phase was demonstrated to be stable under ambient conditions when the particle sizes were reduced to below 10 nm. However, no other phase has been reported to be stable for silver iodides under ambient conditions. Rock-salt and helix structures have been found to be stable under ambient conditions in this study. The structures have been characterized by elemental mapping, Raman scattering, and high-resolution transmission electron microscopy. The stabilities of these structures were also confirmed by molecular dynamics and density functional theory.

**Keywords:** carbon nanotubes, silver iodides, rock salt, helix, ambient conditions

## INTRODUCTION

Silver iodides are widely employed in cloud seeding [1], contrast agents [2], thermo-electrical batteries [3], and medicines [4]. The structure of silver iodides has been demonstrated to be temperature and size dependent. The  $\beta$  phase (II, wurtzite structure) is the most stable structure at temperatures under 420 K. The  $\beta$  and  $\gamma$  phases (II') are usually adopted by silver iodides at ambient conditions, while the  $\alpha$  phase (I, body-centered cubic structure) is more stable for silver iodides when the temperature is higher than 420 K. A melt lattice for silver ions was formed so that the silver ions could transfer inside the crystal lattice; this was called a superionic conductor. In addition to the  $\alpha$  (I),  $\beta$  (II) and  $\gamma$  (II') phases existing at low pressure, there are the rock-salt phase (III), disordered rock-salt phase (III'), tetragonal phase (IV), and KOH-type phase (V) located at high pressure in the  $p$ - $T$  phase diagram [5,6]. The rock-salt phase is adopted for silver iodides at low temperatures with pressures within 400 MPa–11.3 GPa [7–10]. The tetragonal phase is adopted for silver iodides at lower pressure than the rock-salt phase, 300–400 MPa [9]. The V phase has

a structure similar to potassium hydroxide at a much higher pressure—more than 11.3 GPa [10]. The disordered rock-salt phase is adopted at higher temperatures than the rock-salt phase when the pressure is above 600 MPa [5].

It has been demonstrated that the transition temperature for the  $\alpha$  phase decreases with decreasing size of silver iodide crystals, which has been demonstrated to decrease to room temperature [11–15]. However, there is no report about other phase structures of silver iodides. The size of silver iodides can be adjusted to be extremely narrow when encapsulated into the narrow cavities of carbon nanotubes. Different allotropes such as ring-shaped phosphorus [16], diamond nanowires [17], metal nanowires [18], molybdenum disulfide nanowires [19], long carbon chains [20–22], and carbon nanotubes with selective chirality [23–25] have been demonstrated to be produced inside carbon nanotubes.

Herein, we report a way to synthesize rock-salt or helix structures of silver iodides tuned by the inner diameters of carbon nanotubes (CNTs). The silver iodides are encapsulated into multi-walled carbon nanotubes (MWCNTs) with inner diameters of

<sup>1</sup>State Key Laboratory of Electrical Insulation and Power Equipment, Center of

Nanomaterials for Renewable Energy (CNRE), School of Electrical Engineering, Xi'an Jiaotong

University, Xi'an 710049, China;

<sup>2</sup>Department of Physics, Shanghai University, Shanghai 200444, China and

<sup>3</sup>Department of Chemistry and Institute for Advanced Research, Nagoya University, Nagoya 464–8602, Japan

\*Corresponding author. E-mail: [jinying.zhang@mail.xjtu.edu.cn](mailto:jinying.zhang@mail.xjtu.edu.cn)

Received 20

December 2018;

Revised 4 March

2019; Accepted 11

March 2019

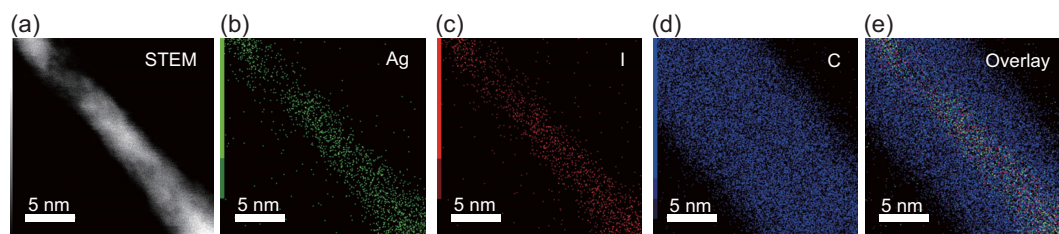


**Figure 1.** EDS mapping of a carbon nanotube filled with silver iodide. (a) High-angle annular dark-field (HAADF) image. (b–d) Elemental mapping of silver, iodine, and carbon respectively. (e) Overlay mapping of silver, iodine, and carbon.

4–8 nm and single-walled carbon nanotubes (SWCNTs) with inner diameters around 1.4 nm. The structures of the encapsulated silver iodides have been demonstrated by Cs-corrected high-resolution transmission electron microscopy (HRTEM), elemental mapping, and Raman scattering. The stability of those structures has also been calculated in dynamics or in energy through molecular dynamics (MD) and density functional theory (DFT) calculations. A stable rock-salt phase structure has been achieved by silver iodides inside MWCNTs with inner diameters of 4–8 nm, while a helix structure has been obtained inside SWCNTs with inner diameters of 1.4 nm, all under ambient conditions.

## RESULTS AND DISCUSSION

The MWCNTs and SWCNTs used were prepared with a chemical vapor deposition (CVD) method [26] and arc discharge method [27], respectively. The silver iodides were sublimed and self-assembled into pre-evacuated nano-cavities of the carbon nanotubes through a vapor-phase transportation method [28] at 773 K for 48 h.

The successful encapsulation of silver iodides inside carbon nanotubes has been well demonstrated by the elemental mapping of Ag, I, and C (Fig. 1) with a field emission scanning transmission electron microscope (FESTEM). The encapsulated structures have much lighter color compared to the surrounding carbon walls (Fig. 1a) due to the higher atomic numbers of Ag and I than C. The distribution of Ag (Fig. 1b) is comparable to that of I (Fig. 1c), which is fully surrounded by carbon atoms (Fig. 1d and e).

The encapsulation of silver iodides into carbon nanotubes was further confirmed by Raman spectra before and after encapsulation (Fig. 2). The G band of MWCNTs was observed to upshift from  $1585\text{ cm}^{-1}$  to  $1589\text{ cm}^{-1}$  after encapsulation due to the hole doping of carbon nanotubes (CNTs) [29] as a result of a large difference in the work functions of the compounds and nanotubes (Fig. 2a).

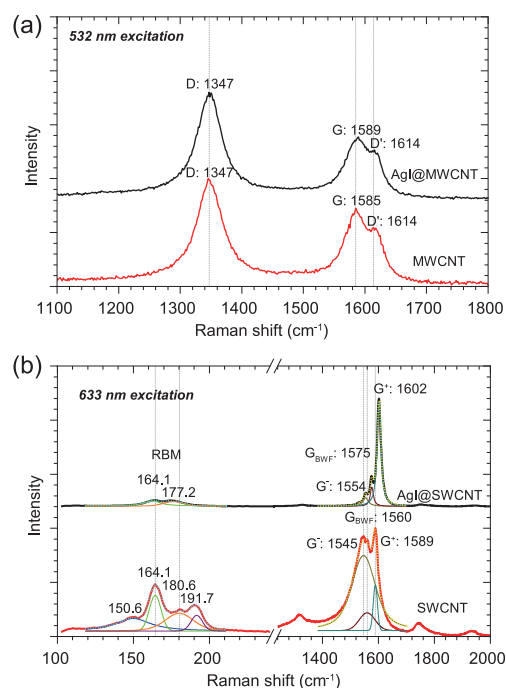


**Figure 2.** Influence on Raman spectra of carbon nanotubes. (a) The spectra of MWCNTs before (black) and after (red) encapsulation of silver iodide. (b) The spectra of SWCNTs before (black) and after (red) encapsulation of silver iodide, along with their peak splitting analyses (blue, green, orange, purple, and cyan for RBM bands; and dark yellow, claret, dark cyan, and yellow for G bands).

The Raman spectra of SWCNTs after encapsulation of silver iodides are easily observed to be different from those of pristine SWCNTs. The Raman spectrum of SWCNTs at the G bands was fitted with the Voigt function and split into three peaks. The  $G^+$  band, corresponding to the longitudinal optic (LO) mode of semiconducting SWCNTs [30], was observed to upshift from  $1589\text{ cm}^{-1}$  to  $1602\text{ cm}^{-1}$  (Fig. 2b, dark cyan), while the  $G_{\text{BWF}}$  band, corresponding to the LO mode of metallic SWCNTs [29, 30], was observed to upshift from  $1560\text{ cm}^{-1}$  to  $1575\text{ cm}^{-1}$  (Fig. 2b, claret), and the  $G^-$  band, corresponding to the transversal optic (TO) mode of semiconducting SWCNTs, was observed to upshift

from  $1545\text{ cm}^{-1}$  to  $1554\text{ cm}^{-1}$  (Fig. 2b, dark yellow). The upshifts of the  $G^+$ ,  $G_{\text{BWF}}$ , and  $G^-$  bands are due to the electron transfer from the SWCNTs to the encapsulated silver iodides. The charge transfer has also been calculated to be about 0.44 electrons per simulation unit (612 C atoms, 30 I atoms, and 30 Ag atoms) through a DFT calculation along with Bader charge analysis [31–34]. The corresponding isosurfaces of simulated charge density differences are shown in Supplementary Fig. 1. The LO mode of SWCNTs was observed to be affected by the encapsulation of silver iodides much more than the TO mode, which is consistent with the reported literature [29]. Analogous to the G bands of SWCNTs, the radial breathing mode (RBM) bands were fitted with the Voigt function and split into four peaks. The first and fourth peaks at  $150.6\text{ cm}^{-1}$  (Fig. 2b, blue) and  $191.7\text{ cm}^{-1}$  (Fig. 2b, purple), corresponding to SWCNTs with chiralities of (20, 1) and (11, 7)/(14, 3), were demonstrated to disappear after the encapsulation of silver iodide (Fig. 2b, purple). The third RBM peak at  $180.6\text{ cm}^{-1}$  (Fig. 2b, orange), corresponding to those with a chirality of (13, 6), was observed to have a weaker intensity and to downshift to  $177.2\text{ cm}^{-1}$ , which might be due to an expansion of the tube diameter. However, the second RBM peak at  $164.1\text{ cm}^{-1}$  (Fig. 2b, green), corresponding to those with chiralities of (14, 7) or (18, 1), was observed to have a weaker intensity without any apparent shift. This consequently led to the conclusion that the most suitable tube diameter of SWCNTs for silver iodide encapsulation is between 1.47 nm and 1.34 nm, since the SWCNTs with inner diameters of 1.47 nm did not show any expansions in the Raman spectrum. This means that it may be the most suitable size for the encapsulation procedure.

The Raman spectra of SWCNTs and MWCNTs before and after encapsulation under both 633 nm and 532 nm excitation are presented in Supplementary Fig. 2. An upshift at the G bands was observed after encapsulation. A downshift at the RBM bands was also observed by the SWCNTs after encapsulation. The difference between the G bands of MWCNTs under different excitations originates from the local thermal effect generated by different kinds of excitations.

The encapsulation yields of AgI into MWCNTs and SWCNTs were also evaluated as more than 85% and 90% respectively through conventional transmission electron microscopy (CTEM) in Supplementary Figs 3 and 4. The crystal structures of the silver iodide encapsulated carbon nanotubes were also characterized by X-ray diffraction (XRD) (Supplementary Fig. 5). Two kinds of MWCNTs, one with open caps where the silver iodides were both deposited inside and outside the MWCNTs

(Supplementary Fig. 5, black) and the other one without open caps where the silver iodides were basically deposited outside the MWCNTs (Supplementary Fig. 5, red), were used for encapsulation. The XRD patterns are similar to each other, being dominated by the inevitable silver iodides ( $\beta/\gamma$ ) deposited outside the carbon nanotubes. No effective method has been obtained to totally get rid of the outer silver iodides.

However, the phase structures of silver iodides encapsulated inside carbon nanotubes are still unclear. More characterizations are necessary to further explore the phase structures of silver iodides inside carbon nanotubes.

The silver iodides inside MWCNTs with inner diameters of 4–8 nm were demonstrated by HRTEM and molecular dynamics (MD) simulations to have a rock-salt lattice structure. HRTEM images of silver iodides inside MWCNTs are shown in Fig. 3a–c. Two perpendicular sets of crystal planes with an interplanar crystal spacing of  $3.0\text{ \AA}$  are observed in Fig. 3a. Both interplanar distances and angles are very consistent with the (0 2 0) and (0 0 2) planes of the rock-salt phase of silver iodides. The HRTEM image is very consistent with the rock-salt structure viewed along  $\langle 1\ 0\ 0 \rangle$  (Fig. 3a, inset). Three sets of crystal planes with an interplanar crystal spacing of  $2.1\text{ \AA}$  and intersected angles of  $60^\circ$  are observed in Fig. 3b, which is very consistent with the (2 -2 0), (2 0 -2), and (0 2 -2) planes of the rock-salt phase of silver iodides, respectively. The HRTEM image is very consistent with the rock-salt structure of silver iodides viewed along  $\langle 1\ 1\ 1 \rangle$  (Fig. 3b). Another two perpendicular sets of crystal planes with interplanar distances of  $3.0\text{ \AA}$  and  $2.1\text{ \AA}$  are observed in Fig. 3c, which is very consistent with the (0 0 2) and (2 -2 0) planes of the rock-salt phase of silver iodides viewed along  $\langle 1\ 1\ 0 \rangle$ . The corresponding structural models are shown in the insets of Fig. 3a–c.

The rock-salt phase of silver iodides inside MWCNTs with inner diameters about 4–8 nm was further confirmed by the simulation results using a MD method [35], where a Parrinello–Rahman–Vashishta (PRV) model [36] was employed to describe the energies between the silver and iodine ions, the Lennard–Jones (LJ) potential [37] was employed to describe the energies between the carbon atoms and silver or iodine ions, and the Tersoff potential [38] was employed to describe the energies between carbon atoms within the carbon nanotubes. A rock-salt phase was obtained for silver iodides encapsulated inside carbon nanotubes with inner diameters of 5.4 nm after annealing and relaxing dynamics, as shown in Fig. 3d and e and Supplementary Fig. 6. A radial distribution function (RDF) was



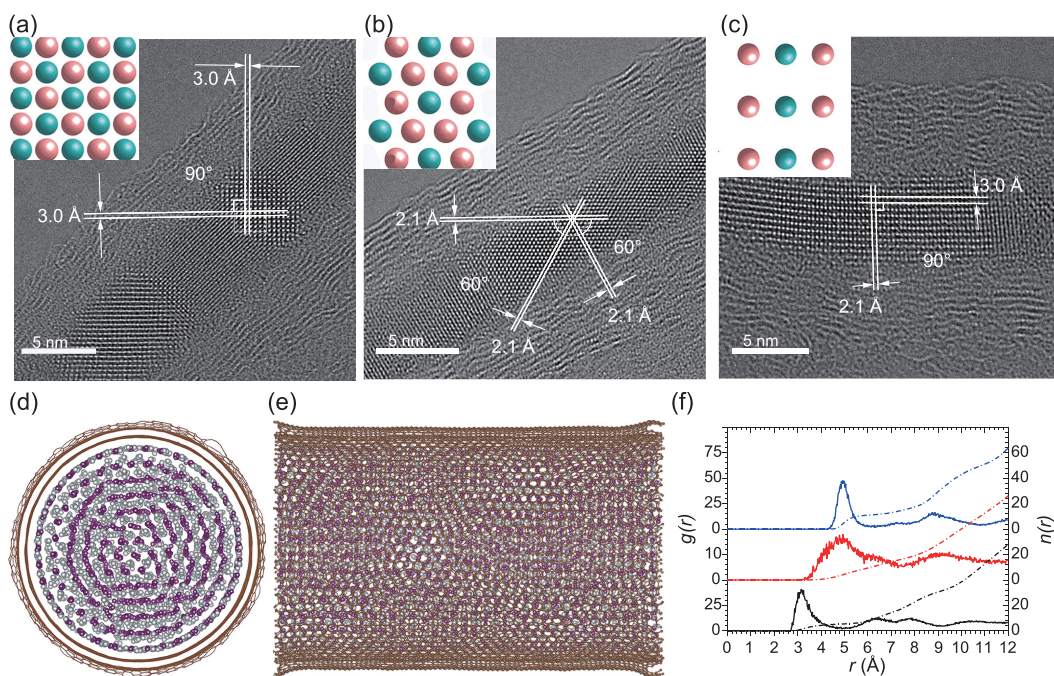


**Figure 3.** Structure characterization of the silver iodide in MWCNTs. HRTEM images of silver iodide inside MWCNTs viewed along different directions with corresponding structural models. (a–c) HRTEM images with corresponding structural models (inset: red—iodine, green—silver) along  $\langle 1\ 0\ 0 \rangle$ ,  $\langle 1\ 1\ 1 \rangle$ , and  $\langle 1\ 1\ 0 \rangle$  respectively. (d, e) The cross section and longitudinal section of the structural model after molecular dynamics simulation. (f) Calculated radial distribution function and average number of neighbors of Ag–I (black line), Ag–Ag (red line) and I–I (blue line) within a sphere of radius  $r$ .

calculated from the structure after MD calculation (Fig. 3f) since the positions of the ions are slightly disordered due to the thermal effect [39]. The same calculation results were obtained when the simulations were also applied to MWCNTs with inner diameters of 4 and 8 nm (Supplementary Fig. 7), confirming that the rock-salt phase was obtained inside MWCNTs with inner diameters between 4 to 8 nm.

The RDF ( $g(r)$  curves) and the  $n(r)$  curves of Ag–I, Ag–Ag, and I–I pairs are shown in Fig. 3f. The  $n(r)$  curve is determined by [40]:

$$n_{ij}(r) = 4\pi\rho_j \int_0^r r^2 g_{ij}(r) dr, \quad (1)$$

where  $i$  and  $j$  refer to the type ions,  $r$  refers to the distance of ions  $i$  from ions  $j$ , and  $\rho_j$  refers to the number of ions  $j$  in a unit volume. It represents the number of ions  $i$  in a sphere of radius  $r$  centered by ions  $j$ .

The value of  $n(r)$  at the first valley of  $g(r)$  refers to the nearest neighbor of  $i$ – $j$  pairs. The average nearest distance of Ag–I pairs was calculated to be 3.15 Å (Fig. 3f, black solid line), slightly bigger than that for the ideal rock-salt phase (3.03 Å) [7,8] due to the size effect of nano-crystals [41], resulting in more surface structures. The nearest distances of Ag–I pairs are 2.83, 2.83, 2.81, and 2.91 Å for the  $\alpha$ ,  $\beta$ ,  $\gamma$ , and tetragonal phases, respectively [10,42,43]. A

rock-salt phase was suggested from the calculated nearest distance of Ag–I pairs. On the other hand, the nearest-neighbor number of Ag–I pairs  $n_{\text{Ag-I}}$  is about 5.5 integrated from the  $g(r)$  curves (Fig. 3f, black dot-dashed line). The nearest-neighbor number of Ag–I pairs is slightly smaller than 6 for the ideal rock-salt phase due to the incomplete edge effects. The nearest-neighbor number of Ag–I pairs is far from 4 for the ideal  $\alpha$ ,  $\beta$  and  $\gamma$ , and tetragonal phases, further confirming the rock-salt phase structures for silver iodides inside MWCNTs. As for the Ag–Ag and I–I pairs, the nearest distances of the four phases were very close to each other, making it difficult to distinguish them from each other (Fig. 3f, red and blue lines). However, from the  $n(r)$  curves, the nearest-neighbor number was determined to be 11.5, close to 12 for the ideal rock-salt phase. The nearest-neighbor numbers are 8, 6, and 4 for the  $\alpha$ ,  $\beta$ , and tetragonal phases, respectively. The nearest-neighbor numbers further confirmed the rock-salt phase for the silver iodides.

A totally different structure from the  $\alpha$  (I),  $\beta$  (II),  $\gamma$  (II'), rock-salt phase (III'), disordered rock-salt phase (III'), tetragonal phase (IV), or KOH-type phase (V) has been observed from the silver iodides encapsulated inside SWCNTs with inner diameters around 1.4 nm. A helix structure was observed from the silver iodides inside SWCNTs by a Cs-corrected

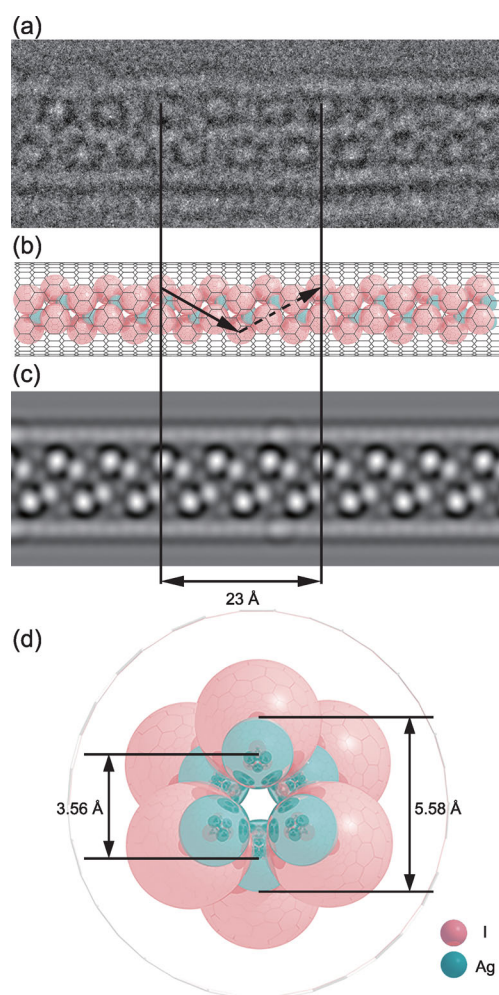


**Figure 4.** Structure characterization of the silver iodide in SWCNTs. (a) HRTEM image of silver iodides encapsulated inside an SWCNT. (b, d) The longitudinal and cross-sectional structural model of silver iodide inside an SWCNT from the DFT calculation. (c) The corresponding simulated TEM image.

HRTEM (Fig. 4a). The helix structure was also obtained by a DFT simulation using the Vienna *ab initio* simulation package (VASP) with exchange correlation function approximated with generalized gradient approximation in Perdew-Burke-Ernzerhof (GGA-PBE) form [44]. The energetically and dynamically stable structure of silver iodides inside an SWCNT with an inner diameter of 1.4 nm is shown in Fig. 4b–d. A triple helix of AgI structure was formed inside SWCNTs with inner diameters around 1.4 nm, where the I ions were located outside of the Ag ions in the radial direction. The diameter of the helix calculated from the I ions is 5.58 Å, while it is 3.56 Å when calculated from the Ag ions (Fig. 4d). The period of the helix along the axial direction is 23 Å. The arrows shown in Fig. 4b are one period of the helix. The simulated TEM image (Fig. 4c)

derived from the calculation results shown in Fig. 4b is very consistent with the observed TEM image (Fig. 4a). The observed helix structure of silver iodides is consistent with reported structures inside SWCNTs [45,46]. However, the structure of the silver iodides inside SWCNTs with inner diameters around 1.4 nm [46] was predicted to be twisted hexagonal structure with theoretical confirmation. The twisted hexagonal structure was also calculated by the DFT method with the same parameters to be unstable in this work (Supplementary Fig. 8), further confirming the structure of silver iodide inside SWCNTs as the helix structure.

However, the structure of silver iodides encapsulated inside SWCNTs with inner diameters around 1.4 nm is totally different from those encapsulated inside MWCNTs with inner diameters of 4–8 nm. The formation of different structures of silver iodides inside carbon nanotubes with different diameters are attributed to the size confinement and quasi-pressure effects of the surrounding carbon nanotube walls. Quasi pressures of 1.9–150 GPa have been predicted by the formations of certain crystal structure of KI [47], FePd<sub>3</sub> [48], Cu [49], Fe [50], and Co [51] inside carbon nanotubes with different diameters. The value depends on the filler structures, temperature and CNT diameters [52]. A quasi pressure of 5 GPa was predicted for nanopores with diameters of 5 nm by grand and semi-grand canonical Monte Carlo simulation [53]. The quasi high pressures provided by carbon nanotubes with diameters of 4–8 nm are between 400 MPa and 11.3 GPa, resulting in the stabilization of rock-salt phases. A quasi pressure around 40 GPa was predicted to be produced inside carbon nanotubes with inner diameters about 1.4 nm [50]. Also, the phase-transition temperatures of high-temperature phases significantly decrease with decreasing size [13]. New phase structures with high temperature and pressures in addition to the exited phase diagram of silver iodides [54] will be formed inside carbon nanotubes with diameters around 1.4 nm, resulting in the formation of helix structures of silver iodides.

The encapsulation method, vaporization in vacuum, was adopted in the formation of different silver iodides. A vapor phase was first produced and then assembled into the carbon nanotubes with different diameters. Different quasi pressures were created inside the carbon nanotubes with different diameters. Different phases in different places of the phase diagram of silver iodides were formed inside carbon nanotubes with different diameters. The nano-size confining effects of carbon nanotubes preserved the as-produced phases at room temperature during cooling to yield the rock-salt and helix structures of silver iodides.

## CONCLUSIONS

Rock-salt and helix structures of silver iodides have been achieved to be stable under ambient conditions by adjusting their diameters using carbon nanotubes with different diameters. A rock-salt phase, which was stable under high pressures of 400 MPa to 11.3 GPa, has been obtained by silver iodides under ambient conditions when the diameters were adjusted to be 4 to 8 nm. A helix structure has been obtained to be stable under ambient conditions when the diameters were decreased to be around 1.4 nm. However, the stable  $\beta$  and  $\gamma$  phases were not observed with narrow diameters up to 10 nm. The silver iodides were self-assembled into rock-salt structures instead of conventional  $\beta$  or  $\gamma$  phases inside MWCNTs with inner diameters of 4–8 nm, while a helix structure instead of any known structures predicted in the  $p$ - $T$  diagram of silver iodides was obtained within SWCNTs with an inner diameter around 1.4 nm. The structure and encapsulation procedure were demonstrated through elemental mapping, Raman scattering, and Cs-corrected HRTEM. The energy or dynamical stability was also verified by MD or DFT calculations.

The properties and applications of the  $\alpha$ ,  $\beta$ , and  $\gamma$  phases have been well investigated. However, very few studies have been reported for rock-salt or other new phases since the structures are not stable at ambient conditions. The rock-salt and helix structures of silver iodides have been achieved to be stable under ambient conditions in this study, which might lead to detailed research on their properties and applications.

## METHODS

### Synthesis of MWCNTs

The MWCNTs were produced by a chemical vapor deposition (CVD) method with Co/Fe- $\text{Al}_2\text{O}_3$  as catalyst and ethylene as carbon source. The amorphous carbon and residual metal catalysts were removed from the pristine MWCNTs by heating in air at 773 K for 1 h and then stirring in 5 wt% HF solutions for 24 h. The samples were then filtered with a 0.45  $\mu\text{m}$  membrane film and washed with deionized water. The as-purified MWCNTs were then dried and collected for further experiments.

### Synthesis of SWCNTs

The SWCNTs were produced by a direct current arc discharge method with a graphite rod containing Ni and Y as anode and a pure graphite rod as cathode. A direct current of 90 A was generated between two

electrodes under a He protective gas at a pressure of 53.33 kPa. The pristine SWCNTs were collected on the inner walls of the arc discharge instrument.

### Synthesis of AgI encapsulated in MWCNTs

The synthesis of AgI encapsulated in MWCNTs was performed through a vapor method. The purified MWCNTs were heated at 773 K for 30 min under an air atmosphere to open the caps. The open-ended MWCNTs were degassed for one day with interval flame heating and then sealed in the presence of extra silver iodide (Sinopharm, CP) under a vacuum of  $10^{-5}$  Pa in a Pyrex tube. The Pyrex tube was then heated to 773 K for 48 h at a heating rate of 1 K/min and then cooled down in an oven.

### Synthesis of AgI encapsulated in SWCNTs

The synthesis of AgI encapsulated in SWCNTs was performed through a vapor method. The SWCNTs were heated at 693 K for 30 min under an air atmosphere to open the caps. The open-ended SWCNTs were degassed for one day with interval flame heating and then sealed in the presence of extra silver iodide (Sinopharm, CP) under a vacuum of  $10^{-5}$  Pa in a Pyrex tube. The Pyrex tube was then heated to 773 K for 48 h at a heating rate of 1 K/min and then cooled down in an oven.

## Material characterization

Raman spectroscopy was taken in a back-scattering geometry using a single monochromator with a microscope (Reinishaw inVia) equipped with a CCD array detector ( $1024 \times 256$  pixels, cooled to 203 K) and an edge filter. The samples were excited by 532 nm and 633 nm argon ion lasers. The spectral resolution and reproducibility was determined to be better than  $0.1 \text{ cm}^{-1}$ . HRTEM images were acquired by FEI TITAN G2 transmission electron microscopy (Cs-TEM; acceleration voltage: 300 kV). CTEM images were acquired by JEM-2100 transmission electron microscopy (TEM; acceleration voltage: 200 kV); elemental mapping of C, I, and Ag was obtained from JEOL JEM-F200 (HR) field emission transmission electron microscopy (FE-TEM; acceleration voltage: 200 kV), equipped with HAADF and EDS modules.

## SUPPLEMENTARY DATA

Supplementary data are available at [NSR](#) online.



## ACKNOWLEDGEMENTS

The STEM and EDS mapping experiments were done at Instrument Analysis Center of Xi'an Jiaotong University. The CTEM and HRTEM image work was done at the International Center for Dielectric Research (ICDR), Xi'an Jiaotong University. The authors thank Mr C. Ma for his help in using TEM. The authors also thank the developers of VASP and LAMMPS, the Henkelman group for the code for the Bader Charge Analysis, and Shanghai Supercomputer Center (SSC) for computing resources.

## FUNDING

This work was supported by the National Natural Science Foundation of China (21771143). J.Z. is supported by the Cyrus Tang Foundation through the Tang Scholar Program.

## AUTHOR CONTRIBUTIONS

J.Z. and H.H. designed the research. Y.Z. and J.H. provided the raw materials. H.H. performed the experiments, analysis, and theoretical calculations. All authors contributed to the discussion and the manuscript.

**Conflict of interest statement.** None declared.

## REFERENCES

1. Guo XL, Zheng GG and Jin DZ. A numerical comparison study of cloud seeding by silver iodide and liquid carbon dioxide. *Atmos Res* 2006; **79**: 183–226.
2. Cong LM, Kobayashi Y and Takeda M *et al.* *Development of Silica Coated Silver Iodide Nano-Particles in Different Sizes for Novel X-Ray Contrast Media*. Singapore: World Scientific, 2006.
3. Kvist A, Randsalu A and Svensson I. Thermoelectric power of solid and molten copper and silver iodide. *Z Naturforsch* 1966; **A21**: 184–5.
4. Kannan M, Rajarathinam K and Venkatesan S *et al.* *Silver Iodide Nanoparticles as an Antibiofilm Agent: A Case Study on Gram-Negative Biofilm-Forming Bacteria*. Amsterdam: Elsevier Science, 2017.
5. Han YH, Wang HB and Troyan IA *et al.* Pressure induced ionic-superionic transition in silver iodide at ambient temperature. *J Chem Phys* 2014; **140**: 044708.
6. Yamamoto T, Maesato M and Hirao N *et al.* The room-temperature superionic conductivity of silver iodide nanoparticles under pressure. *J Am Chem Soc* 2017; **139**: 1392–5.
7. Piermarini GJ and Weir CE. A diamond cell for X-ray diffraction studies at high pressures. *J Res Natl Bur Stans A* 1962; **66**: 325–31.
8. Sowa H. Orientation relations between four phases of AgI. *Z Kristall* 2007; **222**: 89–94.
9. Catti M. Kinetic mechanisms of the pressure-driven phase transitions of AgI. *Phys Rev B* 2005; **72**: 064105.
10. Hull S and Keen DA. Pressure-induced phase transitions in AgCl, AgBr, and AgI. *Phys Rev B* 1999; **59**: 750–61.
11. Binner JGP, Dimitrakis G and Price DM *et al.* Hysteresis in the  $\beta$ - $\alpha$  phase transition in silver iodide. *J Therm Anal Calorim* 2006; **84**: 409–12.
12. Guo YG, Lee JS and Maier J. AgI nanoplates with mesoscopic superionic conductivity at room temperature. *Adv Mater* 2005; **17**: 2815–9.
13. Makiura R, Yonemura T and Yamada T *et al.* Size-controlled stabilization of the superionic phase to room temperature in polymer-coated AgI nanoparticles. *Nat Mater* 2009; **8**: 476–80.
14. Yamasaki S, Yamada T and Kobayashi H *et al.* Preparation of sub-10 nm AgI nanoparticles and a study on their phase transition temperature. *Chem Asian J* 2013; **8**: 73–5.
15. Zhang H, Tsuchiya T and Liang C *et al.* Size-controlled AgI/Ag heteronanowires in highly ordered alumina membranes: superionic phase stabilization and conductivity. *Nano Lett* 2015; **15**: 5161–7.
16. Zhang J, Zhao D and Xiao D *et al.* Assembly of ring-shaped phosphorus within carbon nanotube nanoreactors. *Angew Chem Int Ed* 2017; **56**: 1850–4.
17. Zhang J, Zhu Z and Feng Y *et al.* Evidence of diamond nanowires formed inside carbon nanotubes from diamantane dicarboxylic acid. *Angew Chem Int Ed* 2013; **52**: 3717–21.
18. Kitaura R, Nakanishi R and Saito T *et al.* High-yield synthesis of ultrathin metal nanowires in carbon nanotubes. *Angew Chem Int Ed* 2009; **48**: 8298–302.
19. Wang Z, Li H and Liu Z *et al.* Mixed low-dimensional nanomaterial: 2D ultranarrow MoS<sub>2</sub> inorganic nanoribbons encapsulated in quasi-1D carbon nanotubes. *J Am Chem Soc* 2010; **132**: 13840–7.
20. Shi L, Rohringer P and Suenaga K *et al.* Confined linear carbon chains as a route to bulk carbyne. *Nat Mater* 2016; **15**: 634–9.
21. Zhang J, Feng Y and Ishiwata H *et al.* Synthesis and transformation of linear adamantane assemblies inside carbon nanotubes. *ACS Nano* 2012; **6**: 8674–83.
22. Zhao X, Ando Y and Liu Y *et al.* Carbon nanowire made of a long linear carbon chain inserted inside a multiwalled carbon nanotube. *Phys Rev Lett* 2003; **90**: 187401.
23. Chuvilin A, Bichoutskaia E and Gimenez-Lopez MC *et al.* Self-assembly of a sulphur-terminated graphene nanoribbon within a single-walled carbon nanotube. *Nat Mater* 2011; **10**: 687–92.
24. Zhang J, Zhou F and Miyata Y *et al.* Chirally selective growth and extraction of single-wall carbon nanotubes via fullerene nanopeapods. *RSC Adv* 2013; **3**: 16954–7.
25. Zhang JY, Miyata Y and Kitaura R *et al.* Preferential synthesis and isolation of (6,5) single-wall nanotubes from one-dimensional C<sub>60</sub> coalescence. *Nanoscale* 2011; **3**: 4190–4.
26. Li X, Wang Z and Zhang J *et al.* Carbon nanotube hybrids with MoS<sub>2</sub> and WS<sub>2</sub> synthesized with control of crystal structure and morphology. *Carbon* 2015; **85**: 168–75.
27. Ando Y, Zhao X and Hirahara K *et al.* Mass production of single-wall carbon nanotubes by the arc plasma jet method. *Chem Phys Lett* 2000; **323**: 580–5.
28. Hirahara K, Suenaga K and Bandow S *et al.* One-dimensional metallofullerene crystal generated inside single-walled carbon nanotubes. *Phys Rev Lett* 2000; **85**: 5384–7.
29. Kharlamova MV. Raman spectroscopy study of the doping effect of the encapsulated iron, cobalt, and nickel bromides on single-walled carbon nanotubes. *J Spectrosc* 2015; **2015**: 1–8.

30. Piscanec S, Lazzeri M and Robertson J *et al.* Optical phonons in carbon nanotubes: Kohn anomalies, Peierls distortions, and dynamic effects. *Phys Rev B* 2007; **75**: 035427.
31. Henkelman G, Arnaldsson A and Jónsson H. A fast and robust algorithm for Bader decomposition of charge density. *Comput Mater Sci* 2006; **36**: 354–60.
32. Sanville E, Kenny SD and Smith R *et al.* Improved grid-based algorithm for Bader charge allocation. *J Comput Chem* 2007; **28**: 899–908.
33. Tang W, Sanville E and Henkelman G. A grid-based Bader analysis algorithm without lattice bias. *J Phys: Condens Matter* 2009; **21**: 084204.
34. Yu M and Trinkle DR. Accurate and efficient algorithm for Bader charge integration. *J Chem Phys* 2011; **134**: 064111.
35. Gotlib IY, Ivanov-Schitz AK and Murin IV *et al.* Computer simulation of ionic transport in silver iodide within carbon nanotubes. *Solid State Ion* 2011; **188**: 6–14.
36. Parrinello M, Rahman A and Vashishta P. Structural transitions in superionic conductors. *Phys Rev Lett* 1983; **50**: 1073–6.
37. Baldoni M, Leoni S and Sgamellotti A *et al.* Formation, structure, and polymorphism of novel lowest-dimensional AgI nanoaggregates by encapsulation in carbon nanotubes. *Small* 2007; **3**: 1730–4.
38. Tersoff J. Modeling solid-state chemistry: interatomic potentials for multicomponent systems. *Phys Rev B* 1989; **39**: 5566–8.
39. Matsunaga S. Structure and transport properties of AgI–AgCl–CsCl glasses: molecular dynamics study. *Ionics* 2018; **24**: 1371–6.
40. Toby BH and Egami T. Accuracy of pair distribution function analysis applied to crystalline and non-crystalline materials. *Acta Crystallogr A* 1992; **48**: 336–46.
41. Ya Gamarnik M. The physical nature of changes of lattice parameters in small particles. *Phys Status Solidi B* 1993; **178**: 59–69.
42. Cava RJ, Reidinger F and Wuensch BJ. Single-crystal neutron-diffraction study of AgI between 23° and 300°C. *Solid State Commun* 1977; **24**: 411–6.
43. Moore MJ and Kasper JS. Crystal structure of AgI at 3 kbar. *J Chem Phys* 1968; **48**: 2446–50.
44. Perdew JP, Burke K and Ernzerhof M. Generalized gradient approximation made simple. *Phys Rev Lett* 1996; **77**: 3865–8.
45. Fujimori T, dos Santos RB and Hayashi T *et al.* Formation and properties of selenium double-helices inside double-wall carbon nanotubes: experiment and theory. *ACS Nano* 2013; **7**: 5607–13.
46. Eliseev AA, Yashina LV and Brzhezinskaya MM *et al.* Structure and electronic properties of AgX (X = Cl, Br, I)-intercalated single-walled carbon nanotubes. *Carbon* 2010; **48**: 2708–21.
47. Urita K, Shiga Y and Fujimori T *et al.* Confinement in carbon nanospace-induced production of KI nanocrystals of high-pressure phase. *J Am Chem Soc* 2011; **133**: 10344–7.
48. Boi FS, Du Y and Ivaturi S *et al.* New insights on the magnetic properties of ferromagnetic FePd<sub>3</sub> single-crystals encapsulated inside carbon nanomaterials. *Mater Res Express* 2017; **4**: 035021.
49. Guo Y and Guo W. Structural transformation of partially confined copper nanowires inside defected carbon nanotubes. *Nanotechnology* 2006; **17**: 4726–30.
50. Sun L, Banhart F and Krasheninnikov AV *et al.* Carbon nanotubes as high-pressure cylinders and nanoextruders. *Science* 2006; **312**: 1199–202.
51. Karmakar S, Tyagi PK and Misra DS *et al.* Pressure-induced phase transitions in cobalt-filled multiwalled carbon nanotubes. *Phys Rev B* 2006; **73**: 184119.
52. Guo YF and Guo WL. Structural transformation of partially confined copper nanowires inside defected carbon nanotubes. *Nanotechnology* 2006; **17**: 4726–30.
53. Long Y, Palmer JC and Coasne B *et al.* Under pressure: quasi-high pressure effects in nanopores. *Microporous Mesoporous Mater* 2012; **154**: 19–23.
54. Mellander BE, Bowling JE and Baranowski B. Phase diagram of silver iodide in the pressure range 2.5–10 kbar and the temperature range 4–330°C. *Phys Scripta* 1980; **22**: 541–4.